CASL-U-2015-0178-000

An Azimuthal, Fourier Moment-based Transverse Leakage Approximation for the MPACT 2D/1D Method

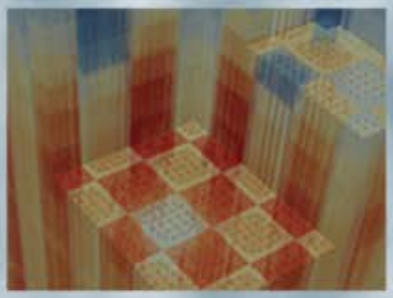

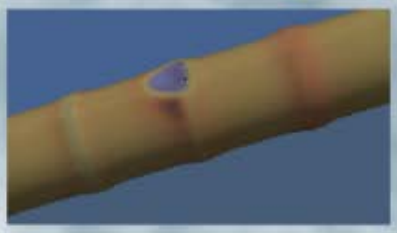

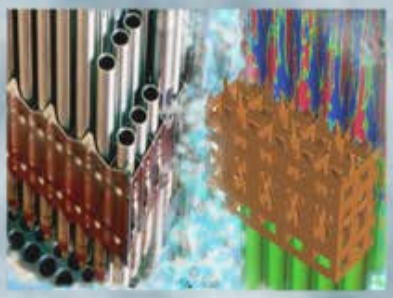

Shane Stimpson, Thomas Downar
University of Michigan

Benjamin Collins,
Oak Ridge National Laboratory

April 19, 2015

CASL-U-2015-0178-000

ANS MC2015 - Joint International Conference on Mathematics and Computation (M&C), Supercomputing in Nuclear Applications (SNA) and the Monte Carlo (MC) Method • Nashville, TN • April 19-23, 2015, on CD-ROM, American Nuclear Society, LaGrange Park, IL (2015)

AN AZIMUTHAL, FOURIER MOMENT-BASED TRANSVERSE LEAKAGE APPROXIMATION FOR THE MPACT 2D/1D METHOD

Shane Stimpson[1], Benjamin Collins[2], and Thomas Downar[1]

[1]Department of Nuclear Engineering and Radiological Sciences
University of Michigan
1901 Cooley Bldg., 2355 Bonisteel Blvd., Ann Arbor, Michigan 48109, USA
sgstim@umich.edu; downar@umich.edu

[2]Oak Ridge National Laboratory
1 Bethel Valley Rd., Oak Ridge, Tennessee 37831, USA
collinsbs@ornl.gov

ABSTRACT

The MPACT code being developed collaboratively by Oak Ridge National Laboratory and the University of Michigan is the primary neutron transport solver within the Virtual Environment for Reactor Applications Core Simulator (VERA-CS). The 2D/1D scheme is the most commonly used method for solving three-dimensional problems. Several axial solvers in this scheme assume isotropic transverse leakages, but work with the axial S_N solver has extended these leakages to include both polar and azimuthal dependence. However, explicit angular representation can be burdensome, both in terms of run time and memory requirements. The work here alleviates this burden by assuming the azimuthal dependence of the angular flux and transverse leakages are represented by the Fourier series expansion. At the heart of this is a new axial S_N solver that takes in a Fourier expanded radial transverse leakage and generates the angular fluxes used to construct the axial transverse leakages used in the 2D-MOC calculations.

These new capabilities are demonstrated for the rodded Takeda LWR benchmark problem and the rodded B configuration of the extended C5G7 benchmark suite. Results with heterogeneous pins, as in the C5G7 benchmark, indicate that cancellation of error between the angular and spatial representation of the transverse leakages may be a factor. To test this, an alternative C5G7 problem has been formulated using homogenized pin cells to reduce the errors introduced by assuming the axial transverse leakage is spatially flat. In both the Takeda and C5G7 problems with homogeneous pins, excellent agreement is observed at fraction of the runtime and signification reductions in memory footprint.

Key Words: azimuthal, Fourier, transverse leakage, 2D/1D, MPACT

1 INTRODUCTION

The Consortium for Advanced Simulation of Light Water Reactors (CASL) [1] is developing the Virtual Environment for Reactor Applications Core Simulator (VERA-CS) [2] which provides multiphysics simulation capabilities for nuclear reactor cores. The primary neutron transport solver of VERA-CS is the MPACT code [3], being developed collaboratively by Oak Ridge National Laboratory (ORNL) and the University of Michigan (UM) and employs the 2D/1D method to solve 3D neutron transport problems [4, 5]. A common approximation used in production level calculations is to assume that the axial and radial transverse leakages

CASL-U-2015-0178-000

that couple the radial and axial solvers are isotropic. Explicitly representing the angular dependence can be particularly burdensome, both in terms of run time and memory footprint. The work presented here investigates the effect of approximating the azimuthal dependence using a Fourier series, including the development of a new axial solver that can properly handle the Fourier moment-based components.

The 2D/1D method with pin-homogenized axial transport and explicit angular dependence of the leakages is very similar to initial work with the "2D/1D Fusion" code CRX at KAIST [6]. Eventually, CRX was modified to perform axial transport on the fine mesh basis, but it was remarked that the memory requirements increased significantly [7]. While the work here focuses on pin-homogenized transport, the approach of using a Fourier expansion to approximate the azimuthal dependence is likely extendable to fine mesh axial transport as well, which would alleviate the memory burden considerably.

Work with a pin-homogenized axial S_N solver in DeCART by Hursin [8, 9] also provided motivation for this work. Hursin investigated incorporating polar dependence into the transverse leakages, by using an azimuthally-integrated variant. Results comparing the NEM and axial S_N solver with these azimuthally-integrated leakages showed promise, indicating that incorporating full angular dependence would be worthwhile.

2 BACKGROUND

2.1 2D/1D

The 2D/1D method is a scheme for solving 3D neutron transport problems by decomposing the geometry into an axial stack of radial planes [4, 5, 10, 11]. In MPACT, 2D-MOC is typically used to solve each radial plane and 1D, pin-homogenized nodal methods are used axially. Historically, diffusion-based solvers (NEM and SENM) have been used [8, 10]. More recently, however, simplified P_N (SP_N) axial solvers have become more standard [5, 11]. This section briefly describes the underlying equations of the radial and axial solvers, as well as identifies some of the approximations that are typical.

2.1.1 Radial equations

To derive the equations for the radial solvers, in which 2D-MOC is employed, the 3D-transport equation is averaged axially, as in Eq. 1:

$$\varphi_{g,l}^{Z}(x,y) = \frac{1}{h_z}\int_{z_B}^{z_T} \varphi_{g,l}(x,y,z)dz. \tag{1}$$

where the axial component of the streaming operator is moved to the right hand side as the axial transverse leakage:

$$\sqrt{1-\mu_l^2}\left(\cos(\alpha_l)\frac{\partial}{\partial x} + \sin(\alpha_l)\frac{\partial}{\partial y}\right)\varphi_{g,l}^{Z}(x,y) + \Sigma_{t,g}^{Z}(x,y)\varphi_{g,l}^{Z}(x,y) = \tilde{q}_{g,l}^{Z}(x,y), \tag{2}$$

$$\tilde{q}_{g,l}^{Z}(x,y) = \bar{q}_{g,l}^{Z}(x,y) + TL_{g,l}^{Z}(x,y).$$

In the above and following equations, g denotes the group index, and l denotes the angle index. In Eq. 2, $\bar{q}_{g,l}^{Z}(x,y)$ denotes the source contribution from scattering and fission (Eq. 3):

$$\bar{q}_{g,l}^{Z}(x,y) = \frac{\chi_g^Z(x,y)}{4\pi k_{\text{eff}}} \sum_{g'=1}^{N_{grp}} \nu\Sigma_{f,g'}^{Z}(x,y)\phi_g^Z(x,y) + \frac{1}{4\pi}\sum_{g'=1}^{N_{grp}} \Sigma_{s0,g'\to g}^{Z}(x,y)\,\phi_{g'}^{Z}(x,y), \tag{3}$$

and one can see that the axial transverse leakage in its most explicit form can be constructed using the angular fluxes at the top and bottom axial interfaces (Eq. 4):

$$TL_{g,l}^{Z}(x,y) = \frac{\mu_l}{h_z}\Big(\varphi_{B,g,l}(x,y) - \varphi_{T,g,l}(x,y)\Big). \tag{4}$$

A simple approximation is to assume that the axial transverse leakage is isotropic, in which case it can be constructed using the net currents at the top and bottom interfaces:

$$TL_{g,l}^{Z}(x,y) = \frac{J_{B,g}(x,y) - J_{T,g}(x,y)}{4\pi h_z}. \tag{5}$$

Additionally, since the axial solves in MPACT are performed on a pin-wise basis, it is assumed that the axial leakage in each fine mesh region in a pin received the same leakage (the shaped is assumed to be flat), where the currents and angular fluxes used to construct the axial leakage are averaged radially over each pin (Eqs. 6 and 7):

$$TL_{g,l}^{Z}(x,y) = \frac{J_{B,g}^{XY} - J_{T,g}^{XY}}{4\pi h_z}, \tag{6}$$

$$TL_{g,l}^{Z}(x,y) = \frac{\mu_l}{h_z}\big(\varphi_{B,g,l}^{XY} - \varphi_{T,g,l}^{XY}\big). \tag{7}$$

2.1.2 Axial equations

Similarly, the equations for the axial solvers can be obtained by averaging the 3D-transport equation radially over both x and y:

$$\varphi_{g,l}^{XY}(z) = \frac{1}{A_{xy}} \int_{y_L}^{y_R} \int_{x_L}^{x_R} \varphi_{g,l}(x,y,z)dxdy. \tag{8}$$

where the radial streaming components are moved to the right hand side:

$$\begin{gathered} \mu_l \frac{d}{dz}\varphi_{g,l}^{XY}(z) + \Sigma_{t,g}^{XY}(z)\varphi_{g,l}^{XY}(z) = \tilde{q}_{g,l}^{XY}(z), \\ \tilde{q}_{g,l}^{XY}(z) = \bar{q}_{g,l}^{XY}(z) + TL_{g,l}^{XY}(z). \end{gathered} \tag{9}$$

Eq. 10 shows the radial transverse leakage, which in explicit form is constructed using the angular fluxes at the left and right boundaries of each pin cell, as calculated by the radial solver:

$$TL_{g,l}^{XY}(z) = -\frac{\sqrt{1-\mu_l^2}}{A_{xy}} \begin{pmatrix} \cos(\alpha_l) \int_{y_L}^{y_R} \Big(\varphi_{g,l}(x_R,y,z) - \varphi_{g,l}(x_L,y,z)\Big)\,dy \\ \sin(\alpha_l) \int_{x_L}^{x_R} \Big(\varphi_{g,l}(x,y_R,z) - \varphi_{g,l}(x,y_L,z)\Big)\,dx \end{pmatrix}. \tag{10}$$

As with the axial transverse leakage, the radial leakage can be assumed to be isotropic and can then be determined using the radial currents on the pin boundaries:

$$TL_{g,l}^{XY}(z) = \frac{1}{4\pi h_x}\Big(J_{L,x,g}(z) - J_{R,x,g}(z)\Big) + \frac{1}{4\pi h_x}\Big(J_{L,y,g}(z) - J_{R,y,g}(z)\Big). \tag{11}$$

In Eqs. 6 and 7, the axial transverse leakage is considered to be flat spatially within each pin. However, because the axial mesh is typically much larger than the radial mesh, a quadratic leakage interpolation scheme is employed using the leakage values from the upper and lower neighbors to construct a more accurate intranodal leakage distribution.

It should be noted that under the right circumstances, the source terms in Eqs. 2 and 9 can become negative, potentially leading the negative fluxes and convergence issues. One means of avoid this is to employ transverse leakage splitting [9], which helps maintain source positivity by moving the transverse leakage term into the total/transport cross section. However, in the cases analyzed in this work, no transverse leakage splitting was necessary to obtain converged solutions.

2.2 Azimuthal, Fourier-Moment Based Transverse Leakages

In Eqs. 4 and 10, the transverse leakages retain explicit dependence on both the azimuthal and polar angles. Eqs. 12 and 13 introduce a Fourier series to account for the azimuthal dependence. For simplicity, these equations are written in terms of continuous angular variables, and $XY||Z$ is used to denote that the approximation can be made to both radially- or axially-averaged quantities.

$$\varphi_g^{XY||Z}(z,\alpha,\mu) = \frac{1}{2\pi}\varphi_{g,0}^{XY||Z}(z,\mu) + \frac{1}{\pi}\sum_{m=1}^{N_{mom}}\Big(\varphi_{g,sm}^{XY||Z}(z,\mu)\sin(m\alpha) + \varphi_{g,cm}^{XY||Z}(z,\mu)\cos(m\alpha)\Big) \tag{12}$$

$$TL_g^{XY||Z}(z,\alpha,\mu) = \frac{1}{2\pi}TL_{g,0}^{XY||Z}(z,\mu) + \frac{1}{\pi}\sum_{m=1}^{N_{mom}}\Big(TL_{g,sm}^{XY||Z}(z,\mu)\sin(m\alpha) + TL_{g,cm}^{XY||Z}(z,\mu)\cos(m\alpha)\Big) \tag{13}$$

In both of these equations, there is a flat component (subscript 0) and a sine and cosine component for each Fourier moment (subgroup sm and cm). A single Fourier moment is considered to have one sine and one cosine moment.

2.2.1 Axial leakages

The coefficients for the Fourier-expanded axial transverse leakage are constructed using the moment-based angular fluxes that are determined by the axial S_N sweeper. These equations look identical to Eq. 4, but with the corresponding moment component of the angular flux:

$$TL_{g,0}^{Z}(z,\mu) = \frac{\mu}{h}\Big(\varphi_{g,0}^{XY}(z_B,\mu) - \varphi_{g,0}^{XY}(z_T,\mu)\Big), \tag{14}$$

$$TL_{g,sm}^{Z}(z,\mu) = \frac{\mu}{h}\Big(\varphi_{g,sm}^{XY}(z_B,\mu) - \varphi_{g,sm}^{XY}(z_T,\mu)\Big), \tag{15}$$

$$TL_{g,cm}^{Z}(z,\mu) = \frac{\mu}{h}\Big(\varphi_{g,cm}^{XY}(z_B,\mu) - \varphi_{g,cm}^{XY}(z_T,\mu)\Big). \tag{16}$$

Since the 2D-MOC solver that uses the axial transverse leakage still explicitly solves all azimuthal and polar angles, the leakage source expansion is evaluated for each angle during the sweep.

2.2.2 Radial leakages

Similarly, the coefficients for the radial transverse leakage expansion are given by Eqs. 17-19. These coefficients are tabulated by the radial solver as it sweeps over all angles explicitly:

$$TL_{g,0}^{XY}(z,\mu) = -\int_0^{2\pi} \frac{\sqrt{1-\mu^2}}{A_{xy}} \left(\begin{array}{l} \cos(\alpha) \int_{y_L}^{y_R} \left(\varphi^Z(x_R,y,\alpha,\mu) - \varphi^Z(x_L,y,\alpha,\mu)\right) dy \\ + \sin(\alpha) \int_{x_L}^{x_R} \left(\varphi^Z(x,y_R,\alpha,\mu) - \varphi^Z(x,y_L,\alpha,\mu)\right) dx \end{array} \right) d\alpha, \tag{17}$$

$$TL_{g,sm}^{XY}(z,\mu) = -\int_0^{2\pi} \sin(m\alpha) \frac{\sqrt{1-\mu^2}}{A_{xy}} \left(\begin{array}{l} \cos(\alpha) \int_{y_L}^{y_R} \left(\varphi^Z(x_R,y,\alpha,\mu) - \varphi^Z(x_L,y,\alpha,\mu)\right) dy \\ + \sin(\alpha) \int_{x_L}^{x_R} \left(\varphi^Z(x,y_R,\alpha,\mu) - \varphi^Z(x,y_L,\alpha,\mu)\right) dx \end{array} \right) d\alpha, \tag{18}$$

$$TL_{g,cm}^{XY}(z,\mu) = -\int_0^{2\pi} \cos(m\alpha) \frac{\sqrt{1-\mu^2}}{A_{xy}} \left(\begin{array}{l} \cos(\alpha) \int_{y_L}^{y_R} \left(\varphi^Z(x,y_R,\alpha,\mu) - \varphi^Z(x,y_L,\alpha,\mu)\right) dy \\ + \sin(\alpha) \int_{x_L}^{x_R} \left(\varphi^Z(x,y_R,\alpha,\mu) - \varphi^Z(x,y_L,\alpha,\mu)\right) dx \end{array} \right) d\alpha. \tag{19}$$

2.3 Axial S_N Solver

The axial S_N solver uses a cubic characteristic formulation to handle the spatial representation [5] and several variations to handle the angular representation. When using isotropic (ISO) or azimuthally-integrated (AZI) radial transverse leakage, only polar angles in the quadrature need to be simulated. With explicit radial leakages, each azimuthal and polar angle needs to be simulated, using an isotropic contribution of the scattering and fission sources as well as the angle-dependent contribution of the leakage. However, the Fourier moment-based axial S_N solver only retains a scattering and fission source components in the zeroth-moment equation (Eq. 20). The corresponding sine and cosine moment equations (Eq. 21 and 22) only contain the leakage component for the source:

$$\mu \frac{\partial}{\partial z} \varphi_{g,0}^{XY}(z,\mu) + \Sigma_{t,g} \varphi_{g,0}^{XY}(z,\mu) = \frac{Q_g^{XY}(z)}{2} + TL_{g,0}^{XY}(z,\mu), \tag{20}$$

$$\mu \frac{\partial}{\partial z} \varphi_{g,sn}^{XY}(z,\mu) + \Sigma_{t,g} \varphi_{g,sn}^{XY}(z,\mu) = TL_{g,sn}^{XY}(z,\mu), \tag{21}$$

$$\mu \frac{\partial}{\partial z} \varphi_{g,cn}^{XY}(z,\mu) + \Sigma_{t,g} \varphi_{g,cn}^{XY}(z,\mu) = TL_{g,cn}^{XY}(z,\mu). \tag{22}$$

These equations produce the necessary angular fluxes to construct the axial transverse leakages described in Eqs. 14 through 16.

3 RESULTS

3.1 Takeda Rodded LWR Benchmark

The first test problem being considered is the Takeda Rodded LWR benchmark [12] that uses a two-group set of cross sections. With symmetry, the problem is a 15 cm cube core surrounded by a 25 cm cube reflector. Next to core is a 5 cm x 5 cm x 25 cm control rod that extends the full height axially. Figure 1 shows the side and top views of the Takeda LWR model.

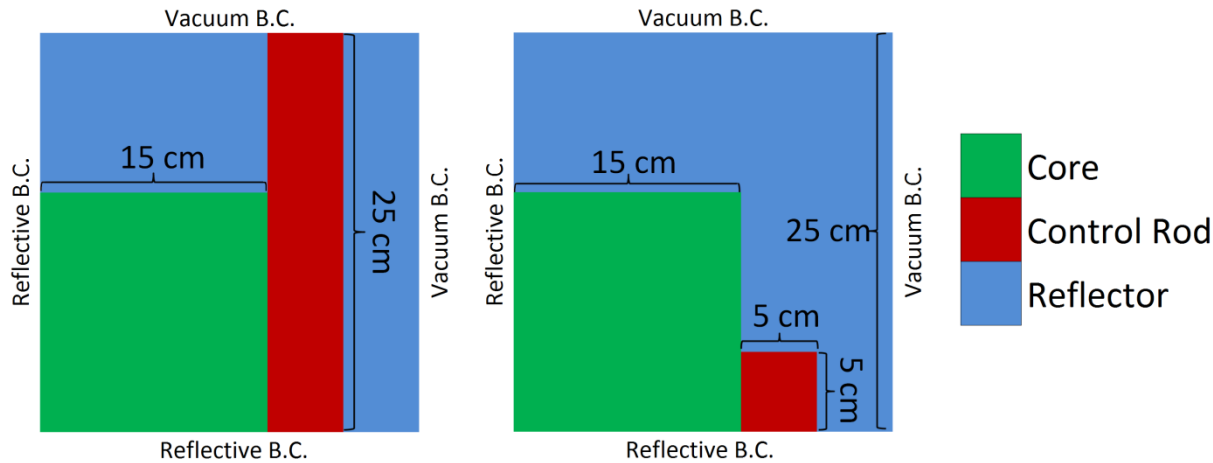

Figure 1. Rodded Takeda Geometry (Side and Top Views)

Table I shows the results for several different axial solvers, including the NEM and NEM-SP_N solvers that use isotropic radial and axial leakages. Additionally, results for the axial S_N solver are shown for several different transverse leakage options, including isotropic (ISO), moment-based (MOM-X), and explicit (EXP). It is important to note that the azimuthally-integrated leakage used by Hursin [8, 9] is most consistent with the MOM-0, which only contains a flat, azimuthally-integrated component without sine or cosine moments.

Table I. Rodded Takeda Eigenvalue, Iterations, and Runtime

Axial Solver	Eigen.	Diff. (pcm)	Iter.	Time (sec)
Reference	0.96240	+/- 60	---	---
NEM (diff.)	0.95002	-1238	17	5.54
NEM-SP_3	0.95504	-736	18	5.61
NEM-SP_5	0.95520	-720	18	5.65
S_N ISO	0.95519	-721	22	6.41
S_N MOM-0	0.95447	-793	22	8.21
S_N MOM-1	0.96282	42	22	9.48
S_N MOM-2	0.96236	-4	22	10.90
S_N MOM-3	0.96240	0	22	12.20
S_N MOM-4	0.96239	-1	22	13.69
S_N EXP	0.96240	0	22	17.38

Table II shows the region-averaged flux distributions for the fuel, reflector, and control rod regions. These fluxes are normalized per Eq. 23. As with the eigenvalue results, the isotropic solvers yield significant errors in the flux distributions, particularly in the reflector region. Incorporating azimuthal dependence significantly reduces these errors.

$$\sum_{g=1}^{2}\left[\int \nu\Sigma_{f,g}(x)\phi_g(x)dV\right] = \sum_{g=1}^{2}\left[\sum_{i=1}^{N_{reg}} \nu\Sigma_{f,g,i}\phi_{g,i}V_i\right] = 1 \tag{23}$$

Table II. Rodded Takeda Flux Comparisons

Axial Solver	Group	Fuel	Reflector	Control Rod
Reference	1	4.7509E-03 (0.10%)	5.9251E-04 (0.21%)	1.4500E-03 (0.47%)
	2	8.6998E-04 (0.12%)	9.1404E-04 (0.23%)	9.7406E-04 (0.63%)
NEM	1	-1.52%	4.71%	-0.02%
	2	0.03%	4.65%	1.44%
SP_3	1	-0.82%	1.79%	-0.24%
	2	-0.09%	2.06%	0.37%
SP_5	1	-0.68%	1.52%	-0.28%
	2	-0.12%	1.88%	0.26%
S_N ISO	1	-0.72%	1.58%	-0.31%
	2	-0.11%	1.86%	0.23%
S_N MOM-0	1	-0.81%	1.93%	0.29%
	2	-0.10%	2.18%	1.16%
S_N MOM-1	1	-0.36%	-0.26%	-0.03%
	2	-0.18%	0.03%	-0.40%
S_N MOM-2	1	-0.42%	-0.05%	0.06%
	2	-0.17%	0.22%	-0.18%
S_N MOM-3	1	-0.41%	-0.08%	0.04%
	2	-0.17%	0.20%	-0.22%
S_N MOM-4	1	-0.41%	-0.07%	0.05%
	2	-0.17%	0.20%	-0.21%
S_N EXP	1	-0.41%	-0.07%	0.05%
	2	-0.17%	0.20%	-0.21%

3.2 3D-C5G7 Extended (Rodded B Configuration)

The next problem under investigation is the C5G7 extended benchmark configuration B [13]. Figure 2 shows the radial pin layout of the core, which contains both UO_2 and MOX fuels.

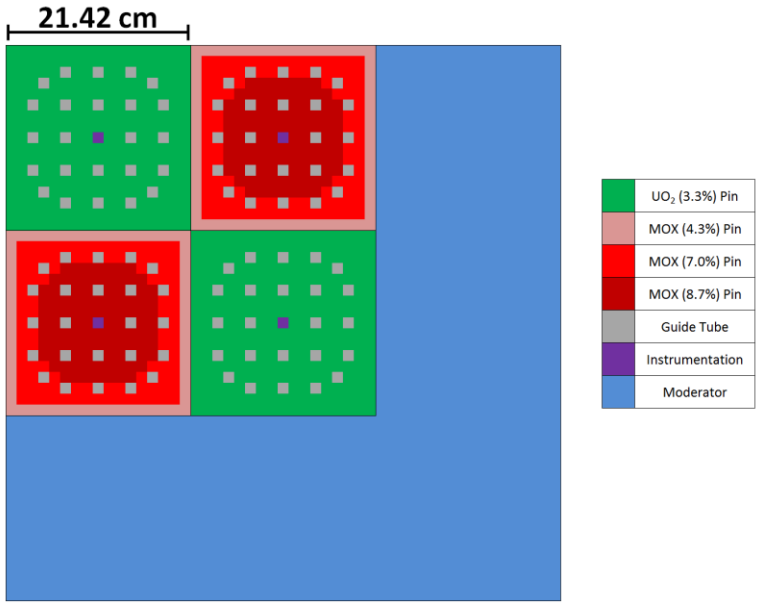

Figure 2. C5G7 Geometry Radial Pin Layout

Figure 3 shows the axial layout of the core with two cross-sectional slices. In the rodded B configuration, the control rod is inserted 28.56 cm into the center UO_2 assembly and 14.28 cm into both of the MOX assemblies. The outer UO_2 assembly remains unrodded, with the rod remaining in the axial reflector above the assembly. The rodded B configuration has been chosen for evaluation because one would expect the azimuthal dependence to be more important in rodded cases.

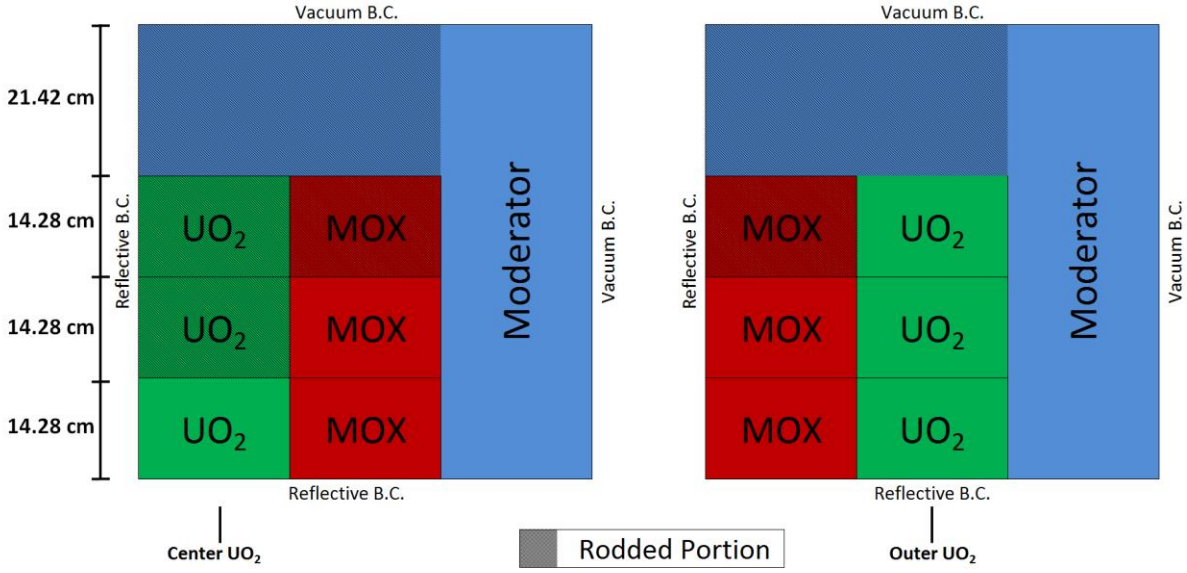

Figure 3. C5G7 Geometry Rodded B Configuration Axial Layout

To ensure the pin power distributions are tightly converged, new reference solutions were obtained using the SHIFT Monte Carlo code [14] using 240 billion histories. The MPACT results were obtained using 0.01 cm ray spacing in a Chebyshev azimuthal quadrature with 16 azimuthal angles and a Gauss-Legendre polar quadrature with 4 polar angles per half-space.

Additionally, unless otherwise specified, a 3.57 cm axial mesh was used. Lastly, all MPACT cases were run on Titan using 648 processors. For the heterogeneous pin cases, a radial mesh of 5 fuel rings and 3 moderator rings with 16 azimuthal divisions was used. Because the homogeneous pins lead to fuel at all corners of each pin, a 15x15 Cartesian sub-meshing was used to more accurately mesh the corners. For consistency with the benchmark, the pin powers were calculated for the three 14.28 cm fuel planes as shown in Figure 3.

3.2.1 Heterogeneous pins

Table III shows the eigenvalue and absolute difference of the pin power results for the standard rodded B configuration with heterogeneous pins with distinct fuel and moderator regions. As expected, the diffusion-based NEM solver is the least accurate with significant errors both in eigenvalue and pin power distribution. The NEM-SP_N and S_N solvers with isotropic leakages significantly improve these errors. However, including azimuthal dependence of the leakages improves the eigenvalue discrepancy, but yields notably higher pin power errors (roughly twice as large as its isotropic counterpart).

Table III. C5G7 Rodded B Configuration Results (Het. Pins)

Axial Solver	Eigen.	Diff. (pcm)	ΔP RMS (%)	ΔP Max (%)	Iter.	Time (min)
MCNP	1.07777	---	---	---	---	---
SHIFT	1.07772	---	---	---	---	---
NEM (diff.)	1.07594	-178	0.77	3.55	7	5.02
NEM-SP_3	1.07701	-71	0.29	0.95	9	5.96
NEM-SP_5	1.07705	-67	0.29	0.94	6	4.51
S_N ISO	1.07701	-71	0.29	0.95	10	6.37
S_N MOM-0	1.07700	-72	0.31	1.02	11	10.55
S_N MOM-1	1.07804	32	0.56	2.31	11	11.29
S_N MOM-2	1.07798	26	0.56	2.28	11	12.40
S_N MOM-3	1.07799	27	0.56	2.29	11	12.94
S_N MOM-4	1.07798	26	0.56	2.29	11	13.90
S_N EXP	1.07798	26	0.56	2.29	11	17.32

By more accurately representing the angular dependence of the leakages and using refined parameters for the quadrature and ray spacing, there is effectively only one major source of error in the spatial representation of the axial leakage, which has been assumed to be flat. To test this, an alternative problem using volume-homogenized, pin-wise cross sections has been formulated to reduce the errors introduced by assuming the axial leakage is flat. SHIFT [14] has also been used to generate a reference solution.

3.2.2 Homogeneous pins

Table IV shows the results for the alternative case with homogeneous pins. The solvers with isotropic leakages yield higher errors than with heterogeneous pins, supporting the idea that cancellation of error is an important factor. While the problem is different, it is not so different

as to expect significant differences in the error distribution. However, now the eigenvalue and pin power errors are very significantly reduced by including azimuthal dependence of the leakages. The pin power errors are roughly three times smaller than with isotropic leakages, and the eigenvalue discrepancy is almost completely removed.

Table IV. C5G7 Rodded B Configuration Results (Hom. Pins)

Axial Solver	Eigen.	Diff. (pcm)	ΔP RMS (%)	ΔP Max (%)	Iter.	Time (min)
SHIFT	1.07468	---	---	---	---	---
NEM (diff.)	1.07241	-227	1.34	6.25	7	5.03
NEM-SP_3	1.07360	-108	0.47	2.24	8	5.45
NEM-SP_5	1.07364	-104	0.44	2.10	8	5.51
S_N ISO	1.07360	-108	0.49	2.37	7	4.89
S_N MOM-0	1.07359	-109	0.48	2.35	10	9.63
S_N MOM-1	1.07470	2	0.15	0.69	11	11.67
S_N MOM-2	1.07464	-4	0.15	0.72	10	11.26
S_N MOM-3	1.07465	-3	0.15	0.71	10	11.94
S_N MOM-4	1.07465	-3	0.15	0.72	10	12.74
S_N EXP	1.07465	-3	0.15	0.72	10	15.83

Figure 4 shows the pin power differences for the S_N solver with isotropic transverse leakages. Not surprisingly, the highest errors are present in the bottom plane, which is along the reflective boundary and has the highest pin powers. Figure 5 shows the results with explicit transverse leakages. With a sufficient number of moments, the moment-based solvers yield nearly identical results. The remaining errors in Fig. 5 can be further reduced by refining the axial mesh.

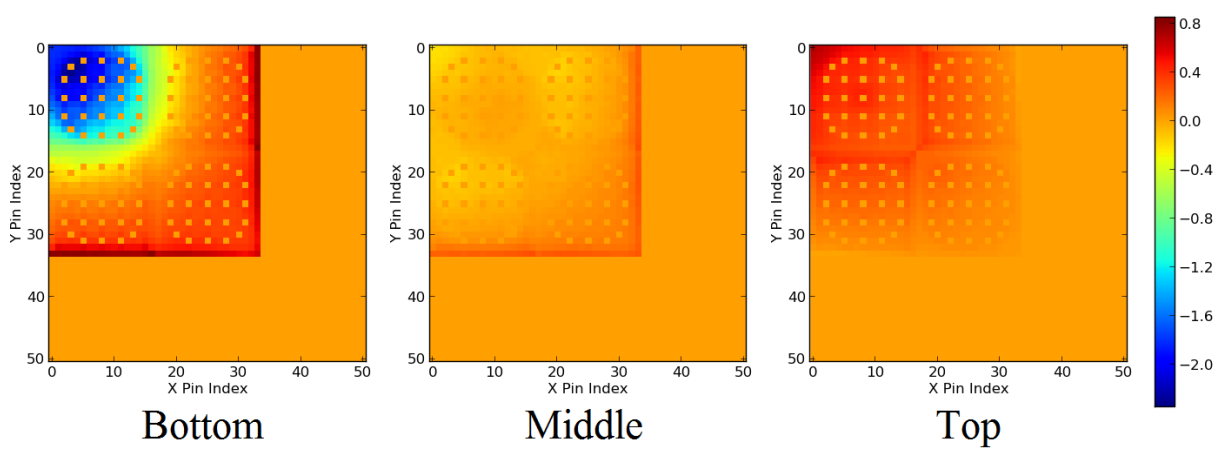

Figure 4. Pin Power Differences, Isotropic Transverse Leakages (3.57 cm Mesh)

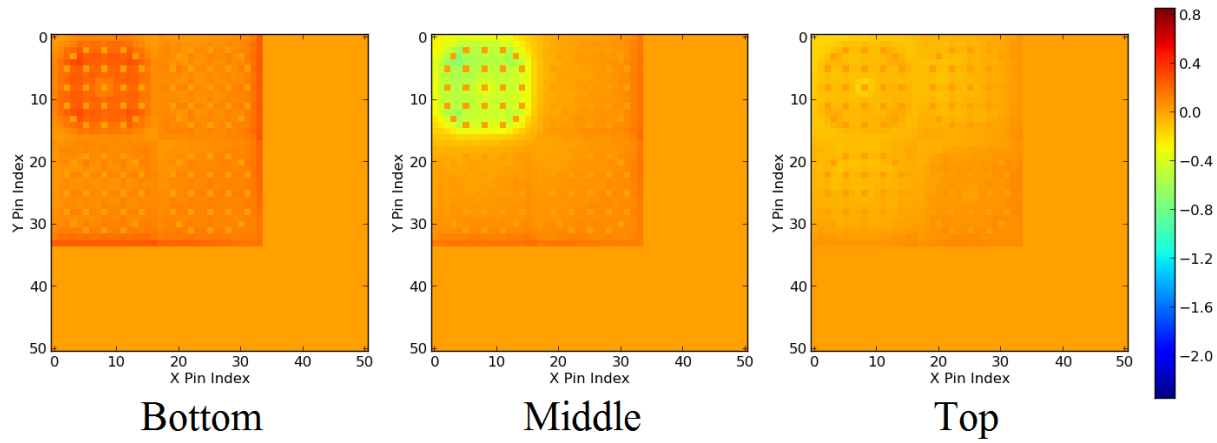

Figure 5. Pin Power Differences, Explicit Transverse Leakages (3.57 cm Mesh)

Table V shows the memory profiling results for the moment-based and explicit solvers for the heterogeneous pin case. As one would expect, the footprint of the angle-dependent memory constructs is reduced by an order of magnitude. Because refined parameters were used, such as ray spacing and radial mesh, there is a significant amount of memory that is unaffected by the Fourier moment approximation. Thus, the overall memory reduction is roughly a factor of 3 or 4 if only one or two Fourier moments are used.

Table V. Angle-Dependent and Total Memory Profile (per plane)

Number of Moments	Angle-Dep. Memory Per Plane (MB)	Total Memory Per Plane (GB)
0	137	1.56
1	291	1.71
2	444	1.86
3	598	2.01
4	752	2.16
Explicit	4,919	6.23

4 CONCLUSIONS

In this work the formulation of a new axial S_N solver was presented that can properly handle the approximation of the radial and axial transverse leakages by a Fourier series. This approximation allows for a significant reduction in the memory footprint and a modest reduction in the overall run time. The new capabilities were demonstrated on the Takeda Rodded LWR benchmark problem and two C5G7 extended benchmark problems. The first C5G7 problem followed the benchmark specification using heterogeneous pins. It was observed that increasing the fidelity of the leakage angular representation yielded larger errors in the pin power distribution. This is suspected to be the result of cancellation of error between the spatial and angular representations of the leakage. To test this, an alternative C5G7 problem was proposed that used pin-homogenized cross sections, making the flat axial leakage approximation more valid and reducing the error introduced by it. In the Takeda benchmark and the new, alternative C5G7 problem the eigenvalue and pin power errors were reduced considerably with higher-order angular representation. In all cases, the Fourier moment-based approach performed well,

suggesting that only one or two Fourier moments are necessary to accurately capture the azimuthal behavior. Additionally, no solution relaxation [15] was used to generate these solutions.

Future work should focus on providing more accurate intrapin spatial distributions for the axial transverse leakage. One option would be to perform axial solves on the fine mesh basis [7], but it may also be possible to accurately represent the shape while still operating on the pin-homogenized basis.

5 ACKNOWLEDGMENTS

The authors wish to express gratitude to the developers SHIFT, which was used to generate reference solutions in this work.

This research was supported by the Consortium for Advanced Simulation of Light Water Reactors (www.casl.gov), an Energy Innovation Hub (http://www.energy.gov/hubs) for Modeling and Simulation of Nuclear Reactors under U.S. Department of Energy Contract No. DE-AC05-00OR22725.

This research also made use of resources of the Oak Ridge Leadership Computing Facility at the Oak Ridge National Laboratory, which is supported by the Office of Science of the U.S. Department of Energy under Contract No. DE-AC05-00OR22725.

6 REFERENCES

1. "Consortium for Advanced Simulation of Light Water Reactors (CASL)," http://www.casl.gov/.
2. S. Palmtag, "Demonstration of Neutronics Coupled to Thermal-Hydraulics for a Full-Core Problem using VERA," CASL-U-2013-0196-000, (December 30 2013).
3. B. Kochunas et al., "Overview of Development and Design of MPACT: Michigan Parallel Characteristics Transport Code," *Proc. M&C 2013*, Sun Valley, ID (May 5-9, 2013).
4. B. Collins et al., "Assessment of 2D/1D Capability in MPACT," *Proc. PHYSOR 2014*, Kyoto, Japan (September 28 – October 3 2014).
5. S. G. Stimpson, B. S. Collins, T. J. Downar, "Axial Transport Solvers for the 2D/1D Scheme in MPACT," *Proc. PHYSOR 2014*, Kyoto, Japan (September 28 - October 3 2014).
6. N. Z. Cho et al., "Refinement of the 2-D/1-D Fusion Method for 3-D Whole-Core Transport Calculation," *Trans. Am. Nucl. Soc.*, Vol. 87, p. 417-420 (2002).
7. G. S. Lee and N. Z. Cho, "2D/1D Fusion method solutions of the three-dimensional OECD benchmark problem C5G7 MOX," *Progress in Nuclear Energy*, **Vol. 48**, p. 410-423, (2006).
8. M. Hursin et al., "The Development and Implementation of a One-Dimensional Sn Method in the 2D-1D Integral Transport Solution," *Nuclear Science and Engineering*, **Vol. 176**, p. 186-200 (2014).
9. M. Hursin, "Full Core, Heterogeneous, Time Dependent Neutron Transport Calculations with the 3D Code DeCART," Ph.D. Dissertation, University of California at Berkeley (2010).

10. H. G. Joo et al., "Methods and Performance of a Three-Dimensional Whole-Core Transport Code DeCART", *Proc. PHYSOR 2004*, American Nuclear Society, Chicago, IL (April 25-29 2004).
11. Y. S. Jung et al., "Practical numerical reactor employing direction whole core neutron transport and subchannel thermal/hydraulic solvers", *Annals of Nuclear Energy*, **Vol. 62**, p. 357-374 (2013).
12. T. Takeda and H. Ikeda, "Final Report on the 3-D Neutron Transport Benchmarks." Tech. Rep. NEA/NEACRP/L(1990)330, Nuclear Energy Agency Organisation for Economic Co-operation and Development (NEA-OECD) (1991).
13. M. A. Smith, E. E. Lewis, and B. C. Na, "Benchmark on Deterministic Transport Calculations Without Spatial Homogenization: MOX Fuel Assembly 3-D Extension Case," Nuclear Energy Agency Organisation for Economic Co-operation and Development (NEA-OECD) (2005).
14. T. Evans et al., "Exnihilo Documentation: Release 5.1 (Dev)," Oak Ridge National Laboratory (August 2014).
15. B. W. Kelley and E. W. Larsen, "2D/1D approximations to the 3D neutron transport equations. I: Theory," *Proc. M&C 2013*, Sun Valley, ID (May 5-9, 2013).